Extreme Materials 2 (2026) 58–68

Contents lists available at ScienceDirect

Extreme Materials

journal homepage: www.keaipublishing.com/en/journals/extreme-materials/

Comparative study of water vapor corrosion resistance in directionally solidified $RE_3Al_5O_{12}/Al_2O_3$ eutectic ceramics at 1500°C: Effect of eutectic structure and rare earth elements

Cui Zhou[a,b], Zhilin Tian[c], Liya Zheng[c], Sikai Wang[b,d], Tiefeng Du[b], Jiemin Wang[b], Bin Yang[b], Min Guo[e], Luchao Sun[b,*], Jingyang Wang[b,*]

[a] Institute of Coating Technology for Hydrogen Gas Turbines, Liaoning Academy of Materials, Shenyang 110016, China
[b] Shenyang National Laboratory for Materials Science, Institute of Metal Research, Chinese Academy of Sciences, Shenyang 110016, China
[c] School of Materials, Shenzhen Campus of Sun Yat-sen University, Shenzhen 518107, China
[d] School of Materials Science and Engineering, University of Science and Technology of China, Shenyang 110016, China
[e] State Key Laboratory of Solidification Processing, Northwestern Polytechnical University, Xi'an 710072, China

ARTICLE INFO

Keywords:
Water vapor corrosion
$RE_3Al_5O_{12}/Al_2O_3$
Eutectic ceramic
Directional solidification

ABSTRACT

Al_2O_3-based directionally solidified eutectic (DSE) ceramics are recognized as promising candidates for high-temperature structural materials in advanced aeroengines. Nevertheless, their corrosion resistance at elevated temperatures continues to pose a critical challenge, limiting broader application in hot-section components. This study investigates corrosion behavior of $RE_3Al_5O_{12}$ (REAG)/Al_2O_3 (RE = rare earth) DSE ceramics in water vapor atmosphere (90 H_2O(g) + 10 vol% air(g)) at 1500°C for durations up to 200 h, with focus on the influence of eutectic structure and RE elements in garnet phases via examining three samples (high-entropy $(Y_{0.2}Gd_{0.2}Ho_{0.2}Er_{0.2}Yb_{0.2})_3Al_5O_{12}$ DSEs fabricated at 10 and 300 mm/h and YAG/Al_2O_3 DSE grown at 10 mm/h). The results indicate that REAG/Al_2O_3 DSE ceramics exhibit excellent water vapor corrosion resistance at 1500°C for up to 200 h, with mass loss values ranging from -0.00757 to -0.00708 mg·cm^{-2}·mg^{-1}. During corrosion, Al_2O_3 phase acts as corrosion-susceptible component compared to REAG phase, with corrosion depth showing a nearly linear relationship with the average Al_2O_3 lamellar width. In addition, garnet phases experience slight grain growth, reducing the contact area between water vapor and Al_2O_3 phase; Gd demonstrates the slowest diffusion rate when compared to other RE elements. Despite these changes, all samples maintain their preferred crystallographic orientations, confirming the structural stability of REAG/Al_2O_3 DSEs under water vapor atmosphere at 1500°C.

1. Introduction

Weight reduction in aircraft delivers multifaceted advantages, including enhanced combustion efficiency, extended service life, reduced exhaust emissions, and lower manufacturing cost. This trend has led to substantially higher performance demands on high-temperature structural materials utilized in hot-end components of aero-engines. Despite advancements in high-temperature structural materials development, long-term operational durability remains a critical challenge under extreme combustion environment, particularly due to severe corrosive exposure such as molten calcium-magnesia-alumina-silicate (CMAS) corrosion [1,2] and high-temperature water vapor corrosion [3,4], especially when operating temperature of aero-engines exceeds 1500°C. Therefore, to meet the stringent requirements of aero-engine hot-end components operating under extreme conditions, such as temperatures exceeding 1500°C and exposure to corrosive environments, it is essential to develop novel high-temperature structural materials.

In 1995, Waku et al. [5] discovered that $Y_3Al_5O_{12}$ (YAG)/Al_2O_3 directionally solidified eutectic (DSE) ceramics can maintain their mechanical strength at elevated temperatures up to 1800°C. Subsequently, extensive investigations have been carried out and confirm that $RE_3Al_5O_{12}$ (REAG)/Al_2O_3 DSE ceramics outstanding potential for high-

Peer review under the responsibility of Editorial Board of Extreme Materials.
* Corresponding authors.
E-mail addresses: lcsun@imr.ac.cn (L. Sun), jywang@imr.ac.cn (J. Wang).

https://doi.org/10.1016/j.exm.2026.100021
Received 21 November 2025; Received in revised form 5 March 2026; Accepted 7 March 2026
Available online 11 March 2026

temperature structural applications due to their exceptional thermal stability, excellent high-temperature strength and inherent oxidation resistance [6–9]. Typically, REAG/Al_2O_3 eutectic ceramics exhibit a coupling growth and a three-dimensionally interpenetrating phase structure characterized by a highly irregular morphology, commonly described as “Chinese script” [10]. This unique microstructure forms a strongly bonded phase interface while effectively eliminating grain boundaries and amorphous boundary phases [11], which is primarily responsible for excellent thermal stability and mechanical performance in high-temperature environments. For instance, $Er_3Al_5O_{12}$ (EAG)/Al_2O_3/ZrO_2 DSE ceramic prepared by laser-heated floating zone method at a growth rate of 25 mm/h exhibited high thermal microstructural stability, showing no detectable microstructural change after exposure to 1600°C for 100 h [12]. Additionally, $GdAlO_3$ (GAP)/Al_2O_3 DSE ceramic fabricated via laser floating zone melting method at under growth rates of 2 μm/s and 100 μm/s demonstrated no significant microstructural coarsening following exposure to 1500°C for 25 h [13]. Moreover, bending strengths of EAG/Al_2O_3 DSE ceramic can reach approximately 2.7 GPa under a growth rate of about 750 mm/h via laser floating zone melting method and remains stable up to 1300 K [14]. Bending strength of YAG/Al_2O_3/ZrO_2 eutectic ceramic, fabricated by hot isostatic pressing at 1550°C under a pressure of 200 MPa for 60 min, was maintained at 299.38 MPa after exposure to 1500°C, corresponding to a strength retention rate of 84.81% [15]. Furthermore, high-temperature structural components in aero-engines are routinely subjected to severe operating conditions characterized by elevated temperatures, exposure to molten calcium-magnesia-alumina-silicate (CMAS) deposits and high concentrations of water vapor, which collectively contribute to accelerated material degradation. Previous studies have investigated the resistance of YAG/Al_2O_3 DSE ceramics to CMAS corrosion at 1500°C, demonstrating that YAG/Al_2O_3 DSE ceramics possess excellent resistance to CMAS attack [16–18]. Additionally, Bahlawane et al. [19] and Otsuka et al. [20] have reported that YAG/Al_2O_3 DSE ceramic exposed to a humid atmosphere at temperatures up to 1700°C exhibit only slight changes in weight and volume, demonstrating their considerable potential for application as high-temperature structural components in aero-engine hot-end sections.

Previously, we successfully developed a novel directionally solidified $(Y_{0.2}Gd_{0.2}Ho_{0.2}Er_{0.2}Yb_{0.2})_3Al_5O_{12}/Al_2O_3$ (hereinafter referred to as $(5RE_{0.2})AG/Al_2O_3$) ceramic via OFZM method incorporating high-entropy design. This high-entropy composite demonstrates a markedly enhanced capability to form a stable crystallographic texture, achieving this within a significantly shortened growth distance of less than 15 mm. This stands in sharp contrast to its counterparts containing a single rare-earth element, which typically requires a growth distance of 80 mm or more [21]. Furthermore, $(5RE_{0.2})AG/Al_2O_3$ DSE ceramic exhibits excellent mechanical properties, including a Vicker’s hardness of 16.5 ± 0.1 GPa and a fracture toughness of 3.4 ± 0.3 MPa·$m^{1/2}$, as well as notable resistance to CMAS corrosion, with a true recession depth about 219.5 μm after exposure to CMAS at 1500°C for 200 h [22]. Nevertheless, the corrosion behavior and the underlying degradation mechanism of $(5RE_{0.2})AG/Al_2O_3$ DSE ceramics under high-temperature water vapor conditions, one of the most critical degradation mechanisms in aero-engine combustion environments, remain not fully elucidated. For both accurately assessing the corrosion resistance and comprehensively understanding the corrosion mechanisms of $(5RE_{0.2})AG/Al_2O_3$ DSE ceramic in high-temperature water vapor environments, two critical aspects consequently require focused investigation. The first one is the influence of eutectic interface. As reported by Otsuka et al., the weight loss of YAG/Al_2O_3 DSE ceramic is accompanied by interfacial instability between YAG phase and Al_2O_3 phase under a water vapor content of 0.03% [19]. However, the interface between eutectic phases cannot be avoided and significantly influences both their fabrication and mechanical characteristics in directionally solidified eutectic ceramics [21–25]. The second point to consider is the impact of the high-entropy design introduced in $(5RE_{0.2})AG/Al_2O_3$ DSE. For high-entropy design of ceramic materials, driven by four core effects encompassing high-entropy effect, slow diffusion effect, lattice distortion effect, and cocktail effect [23–26], has emerged as a promising strategy in materials engineering. This approach enables the integration of multiple distinctive properties, surpassing the performance of individual components and offering substantial potential for microstructural control and optimization of key material characteristics, including high-temperature water vapor corrosion resistance [27–29]. For example, Dong et al. [30] investigated that high-entropy $(Yb_{0.2}Y_{0.2}Lu_{0.2}Sc_{0.2}Gd_{0.2})_2Si_2O_7$ exhibited a weight gain of approximately 3.7×10^{-4} mg/cm^2 after exposure to an atmosphere containing 50 H_2O and 50 vol% O_2 at 1400°C for 200 h, representing a reduction of several orders of magnitude compared to single-component rare earth disilicates. Additionally, weight loss of high-entropy $(Lu_{0.2}Yb_{0.2}Er_{0.2}Tm_{0.2}Sc_{0.2})_2Si_2O_7$ was significantly lower than that of single-component $RE_2Si_2O_7$ (where RE = Lu, Yb, Er, Tm or Sc) [31]. Therefore, the impact of multi-rare-earth principal element design on high-temperature water vapor performance in $(5RE_{0.2})AG/Al_2O_3$ DSE ceramics, along with the distinct roles of individual rare-earth elements, requires further investigation.

Based on the aforementioned foundations, this study further investigated the water vapor corrosion behavior of REAG/Al_2O_3 DSE ceramics at 1500°C, including high-entropy $(5RE_{0.2})AG/Al_2O_3$ fabricated at growth rates under 10 mm/h and 300 mm/h, as well as YAG/Al_2O_3 fabricated at 10 mm/h, hereafter referred to as 10HE, 300HE and 10YA, respectively. These DSE ceramics function as comparative systems featuring intentionally designed variations in eutectic interspacing and rare-earth constituent elements within the garnet phase, specifically to probe the effects of interface characteristics and compositional design on high-temperature corrosion behavior of REAG/Al_2O_3 DSEs. The water vapor corrosion tests were carried out at 1500°C for durations up to 200 h under an atmosphere composed of 90 $H_2O_{(g)}$ and 10 vol% $Air_{(g)}$, with samples extracted at regular intervals of every 50 h for analysis. Furthermore, the influence of the microstructure characteristics, including eutectic interspacing and crystallographic orientation relationship, on water vapor corrosion resistance of REAG/Al_2O_3 DSE ceramics under these conditions was assessed. Based on the results we obtained here, we hope to elucidate the corrosion mechanism of REAG/Al_2O_3 DSE ceramics under high-temperature water vapor conditions, thereby providing theoretical insights for subsequent improvement the resistance of REAG/Al_2O_3 DSE ceramics to water vapor corrosion.

2. Experiments

2.1. Sample fabrication

Commercially available RE_2O_3 (RE = Y, Gd, Ho, Er and Yb) (99.9%, Dingnan Dahua New Materials Resources Co., Ltd., Jiangxi, China) and Al_2O_3 (Sinopharm Chemical Reagent Co., Ltd., Shanghai, China) were employed as raw materials for the fabrication of high-entropy $(5RE_{0.2})AG/Al_2O_3$ and YAG/Al_2O_3 DSE ceramics. RE_2O_3 and Al_2O_3 powders were homogeneously mixed in a molar ratio of 18:82 [32], corresponding to the eutectic composition of YAG/Al_2O_3. Additionally, in high-entropy $(5RE_{0.2})AG/Al_2O_3$ DSE ceramics, the five RE_2O_3 powders were mixed in equimolar proportions. Calculations were carried out based on the molar ratio of high-entropy eutectic ceramics and the relative molecular masses of RE_2O_3 and Al_2O_3. The raw powders were proportioned in accordance with the mass ratio of Y_2O_3:Gd_2O_3:Ho_2O_3:Er_2O_3:Yb_2O_3:Al_2O_3, which was 6:9:9:10:10:56. Then, the raw powders were homogenized via ball milling using ethanol as a solvent for 6 h in a Si_3N_4 jar with Si_3N_4 balls, yielding a homogeneous slurry. The slurry was subsequently dried at 60–70°C for 12 h and then sieved though an 80-mesh sieve to obtain homogeneously mixed powders. The as-prepared mixed powders were dry-pressed into a steel mold under a pressure of 25 MPa for 30 s, yielding a rectangular-

shaped sample with approximate dimensions of 120 × 15 × 15 mm^3. Subsequently, the rectangular-shaped samples were subjected to cold isostatic pressed at 275 MPa for 10 min, followed by pressureless sintering at 1550°C for 10 h. The resulting rod was directionally solidified using an optical floating zone melting furnace. A polycrystalline Al_2O_3 rod was employed as seed crystal. The growth rates in the high-entropy $(5RE_{0.2})AG/Al_2O_3$ DSE ceramics were controlled at 10 mm/h and 300 mm/h hereinafter referred to as 10HE and 300HE, respectively, whereas growth rate of YAG/Al_2O_3 DSE ceramic was maintained at 10 mm/h as reference group, denoted as 10YA. Directional solidification experiments were conducted in an optical floating zone furnace equipped with four 3 kW xenon lamps serving as heat sources [33]. The heat emitted by four xenon lamps was concentrated onto a single point by four ellipsoidal mirrors, leading to the melting of preform and formation of a suspended droplet. To guarantee the stability of floating zone, upper and lower fixtures were rotated in opposite directions. Consequently, $REAG/Al_2O_3$ DSE ceramics after directional solidification treatment appeared as rod-shaped samples.

2.2. Water vapor corrosion test

The samples for water vapor corrosion test were machined into rectangular blocks with dimensions of 5 × 5 × 4 mm^3. The surfaces designated for exposure to water vapor were polished to a 1-μm finish to ensure smoothness and eliminate defects, followed by ultrasonic cleaning in anhydrous ethanol. Corrosion tests were conducted over periods up to 200 h at a temperature of 1500°C in a quasi-static high-temperature water vapor environment. To gain a comprehensive understanding of the behavior of water vapor in high-entropy $(5RE_{0.2})AG/Al_2O_3$ and single-component YAG/Al_2O_3 DSE ceramics, multiple analytical techniques were utilized to examine the corroded surfaces following exposure to water vapor at 1500°C for durations of 50, 100, 150 and 200 h. Moreover, the cross-sectional morphology of high-entropy $(5RE_{0.2})AG/Al_2O_3$ and single-component YAG/Al_2O_3 DSE ceramics after exposure to water vapor at 1500°C for 200 h was analyzed to investigate interfacial corrosion behavior. The experimental setup comprised a vertical vacuum atmosphere tube furnace (GSL-1600X, Zhengzhou Kejing Furnace Co., Ltd., Henan, China) equipped with a 99% pure Al_2O_3 ceramic tube and a steam vapor evaporation mixer. According to the accelerated water vapor corrosion test protocol published by National Aeronautics and Space Administration (NASA) of the United States [34], the test environment employs a gas mixture consisting of 90 $H_2O_{(g)}$ and 10 vol% $Air_{(g)}$. Additionally, gas flow rate was maintained at 80 cm/s. Reverse osmosis water was heated to 120°C to ensure complete vaporization prior to entering the furnace, thereby preventing condensation on the inner surface of piping.

2.3. Characterization

The mass changes of 10HE, 300HE and 10YA before and after exposure to water vapor corrosion environment for varying durations were measured using an electronic analytical balance (BSA124S, Sartorius, Göttingen, Germany). The resistance of materials to water vapor corrosion was evaluated based on the weight change per unit area. It is noteworthy that, considering the density differences among three samples involved in this study, mass loss per unit mass and per unit area ΔW ($mg{\cdot}cm^2{\cdot}mg^{-1}$) was employed for comparing resistance of water vapor corrosion. The phase compositions of samples before and after exposure to water vapor for varying durations were characterized using X-ray diffraction (D8 Advance, Bruker, Berlin, Germany) and high-resolution field emission scanning electron microscope (Tescan Clara, Tescan, Brno, Czech Republic) equipped with an energy-dispersive X-ray spectroscopy (EDS) system. The surface morphology of three samples prior to and following water vapor corrosion treatment, as well as the cross-sectional morphology of three samples after 200 h of exposure to water vapor corrosion at 1500°C, was observed using a field emission scanning electron microscope (SEM5000X, Guoyi Quantum Science & Technology Co., Ltd., Anhui, China) to investigate microstructural alterations. The crystallographic characteristics of garnet phase ($(5RE_{0.2})AG$ and YAG) in three samples, both before and after exposure to water vapor corrosion at 1500°C, were analyzed using electron backscatter diffraction (EBSD) with a SymmetryS3 detector (Oxford Instruments, Oxfordshire, UK). To evaluate changes in surface roughness, surface roughness variations in three samples were quantitatively assessed using a laser scanning confocal microscope (LEXT OLS5100, Olympus, Tokyo, Japan).

3. Results and discussion

3.1. Weight loss

To investigate the influence of eutectic interspacing on water vapor corrosion resistance of $REAG/Al_2O_3$ eutectic ceramics, two types of high-entropy $(5RE_{0.2})AG/Al_2O_3$ eutectic ceramics with significantly different average lamellar widths of REAG and Al_2O_3 phases were fabricated under growth rates of 300 mm/h (300HE) and 10 mm/h (10HE) achievable with OFZM technique. Additionally, to evaluate the effect of high entropy design of garnet phase on water vapor corrosion behavior, YAG/Al_2O_3 eutectic ceramics grown at a rate of 10 mm/h (10YA) were selected for comparative analysis. Fig. 1 presents the macroscopic images of 10HE, 300HE and 10YA before and after undergoing 200 h of water vapor corrosion at 1500°C under an atmosphere consisting of 90 H_2O and 10 vol% air. A comparative analysis of the microscopic images of 10HE before and after water vapor test reveals that 10HE undergoes only a macroscopic color transition from blue to pink, with no notable structural and morphological alterations observed. This phenomenon can be primarily attributed to the elimination of oxygen vacancies during the initial 50 h of exposure to water vapor at 1500°C, which has also been observed in $GdAlO_3/Al_2O_3/ZrO_2$ DSE ceramic fabricated via laser 3D printing in previous studies [35]. Additionally, no significant macroscopic corrosion features were observed on surface of 10HE during the subsequent exposure period (50–200 h), as illustrated in Fig. 1(b-e). Likewise, no notable macroscopic corrosion was detected on 300HE and 10YA, either before or after the entire water vapor corrosion testing process, as shown in Fig. 1(a-e). These results demonstrate that the $REAG/Al_2O_3$ DSE ceramics maintain macroscopic stability under exposure to water vapor at 1500°C, with no observable defects formation, such as cracks and holes, or structural collapse throughout the exposure period.

The time-dependent mass changes of 10HE, 300HE and 10YA samples were determined during exposure to water vapor corrosion at 1500°C, as illustrated in Fig. 2. The corresponding surface SEM micrographs of these samples before and after exposure to water vapor corrosion at 1500°C are also presented as insets in Fig. 2. It can be observed that the masses of 10HE, 300HE and 10YA samples progressively decreased over time when exposed to a high-temperature gas environment containing 90 H_2O and 10 vol% air. Additionally, after 50 h of exposure to water vapor at 1500°C,

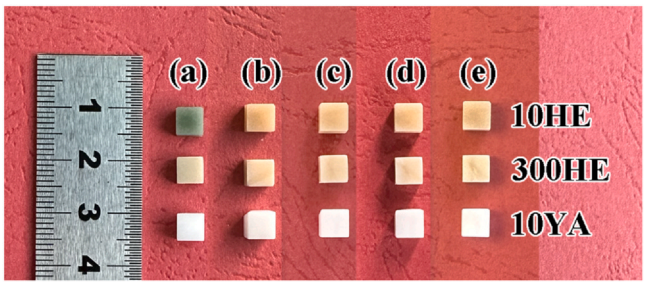

Fig. 1. Macroscopic images of 10HE, 300HE and 10YA various samples after exposure to water vapor corrosion at 1500°C for: (a) 0 h, (b) 50 h, (c) 100 h, (d) 150 h and (e) 200 h.

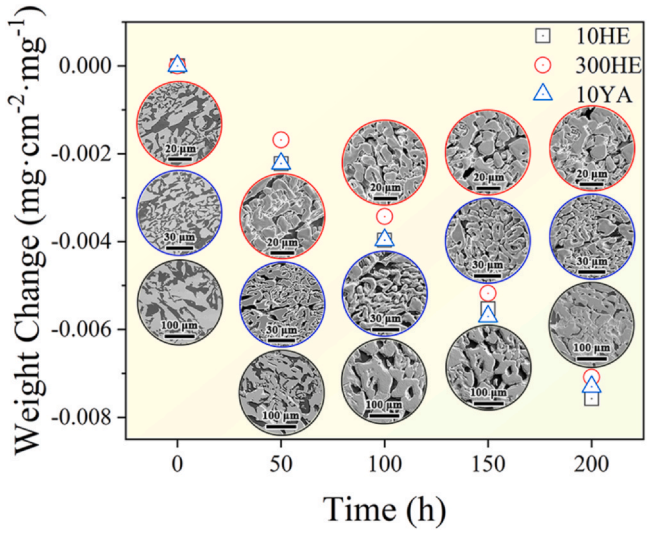

Fig. 2. Mass change plots versus corrosion time of 10HE, 300HE and 10YA, together with the surface SEM micrographs of these samples before and after exposure to water vapor corrosion at 1500°C (insets).

three samples demonstrated a reduction in mass, primarily due to corrosion and consumption of surface dark phase during initial 50-hour exposure period, as illustrated in the insets of Fig. 2. With prolonged exposure, dark phase on surface will continue to be consumed over time, which is accompanied by a further wight loss. Furthermore, the measured weight changes after 200 h of exposure were determined to be $-0.00757\ mg{\cdot}cm^{-2}{\cdot}mg^{-1}$ for 10HE, $-0.00708\ mg{\cdot}cm^{-2}{\cdot}mg^{-1}$ for 300HE and $-0.00730\ mg{\cdot}cm^{-2}{\cdot}mg^{-1}$ for 10YA, respectively. These results demonstrate that 300HE exhibits the highest resistance to water vapor corrosion under testing conditions for up to 200 h. Subsequently, 10YA follows, whereas 10HE demonstrates the lowest performance with the greatest weight loss. Nevertheless, the differences in weight loss among three samples (10HE, 300HE and 10YA) were not significant. What should be mentioned is that the 10HE sample exhibited the highest weight loss rate (1.74×10^{-5} g/(cm^2·h)) among the three samples. However, this value remains significantly lower than that of $Yb_2Si_2O_7$ (7.5×10^{-4} g/(cm^2·h)), which was exposed to a 1500°C environment with 30 wt% water vapor [36]. Importantly, the water vapor content in this environment was substantially lower than that in our experiment. These results demonstrate that REAG/Al_2O_3 DSE ceramics exhibit excellent resistance to water vapor corrosion at temperatures up to 1500°C.

3.2. Phase evolution

The XRD patterns of 10HE, 300HE and 10YA samples before and after exposure to water vapor corrosion at 1500°C for 50, 100, 150 and 200 h are shown in Fig. 3. Prior to water vapor corrosion, the surface of 10HE sample consists exclusively of peaks corresponding to (5RE$_{0.2}$)AG phase and Al_2O_3 phase, as shown in Fig. 3(a). Following exposure to water vapor corrosion at 1500°C, the diffraction intensity of certain Al_2O_3 peaks demonstrates a significant reduction, including those corresponding to (110) and (113) marked with a gray box in Fig. 3(a). When duration of water vapor corrosion reaches 200 h, 10HE sample still contains only diffraction peaks corresponding to (5RE$_{0.2}$)AG phase and Al_2O_3 phase, with relatively low intensity of Al_2O_3 peaks, indicating a relatively low content of Al_2O_3 phase in 10HE sample surface. As illustrated in Fig. 3(b), only (5RE$_{0.2}$)AG phase and Al_2O_3 phase are detected in 300HE sample before and after exposure to water vapor corrosion at 1500°C. Notably, (300) diffraction peak of Al_2O_3 phase in 300HE sample exhibits the highest intensity and demonstrates a gradual decrease over time. Meanwhile, as presented in Fig. 3(c), only YAG phase and Al_2O_3 phase are detected before and after water vapor corrosion at 1500°C. These results indicate that no solid corrosion products are formed in REAG/Al_2O_3 DSE ceramics when exposed to water vapor at 1500°C.

3.3. Surface microstructure

The morphologies of a presentive area on the surface of 10HE before and after exposure to water vapor corrosion at 1500°C are presented in Fig. 4. Specifically, Fig. 4(a) illustrates the microstructural characteristics of 10HE prior to water vapor exposure. The microstructure exhibits an irregular eutectic structure with a morphology resembling a "Chinese Script". This structure is formed via mutually entangled and coupled growth of grey and black phases, attributed to Jackson factor of their constituent phases being greater than 5. EDS analysis reveals that the grey regions correspond to (5RE$_{0.2}$)AG phase, with an approximate atomic ratio of RE:Al of 3:5.1; whereas the dark areas represent Al_2O_3 phases, with an approximate atomic ratio of Al:O of 2:2.8. Fig. 4(b1-b4) provides a magnified view of the region marked by yellow dashed box (b) in Fig. 4(a) after water vapor corrosion at 1500°C for 50, 100, 150 and 200 h, respectively. This region is situated near the center of 10HE surface. As shown in Fig. 4(b1), following initial 50-hour exposure to water vapor corrosion at 1500°C, the surface of 10HE sample exhibits a reduction in Al_2O_3 phase, formation of corrosion pits, and increased roughness within the coarse (5RE$_{0.2}$)AG phase. A comparison of surface morphology of 10HE before and after exposure to water vapor at 1500°C for 50–200 h, as shown in Fig. 4, reveals that corrosion of Al_2O_3 phase results in a reduction in sizes (as indicated by light cyan boxes) or the formation of corrosion pits (as indicated by light green boxes). As highlighted in previous literature [37], Al_2O_3 can react with water vapor at elevated temperatures, leading to the formation of gaseous Al(OH)$_3$ and subsequent material degradation, as described by following reaction: $Al_2O_{3(s)}+3H_2O_{(g)}\rightarrow 2Al(OH)_{3(g)}$. In contrast, (5RE$_{0.2}$)AG phase remains relatively highly stability, maintaining two distinct

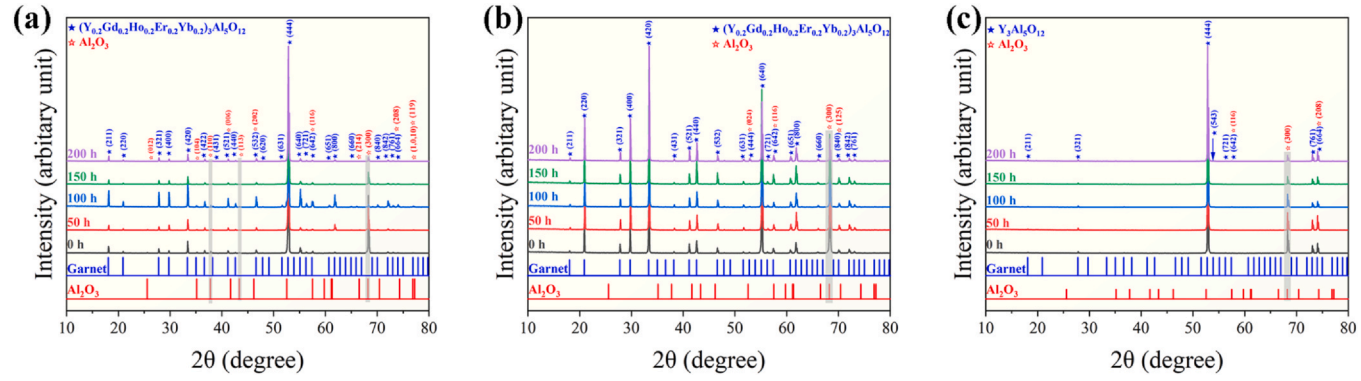

Fig. 3. XRD patterns of surface of three different samples before and after exposure to water vapor corrosion at 1500°C for 200 h under an atmosphere composed of 90 H_2O and 10 vol% air: (a) 10HE, (b) 300HE and (c) 10YA.

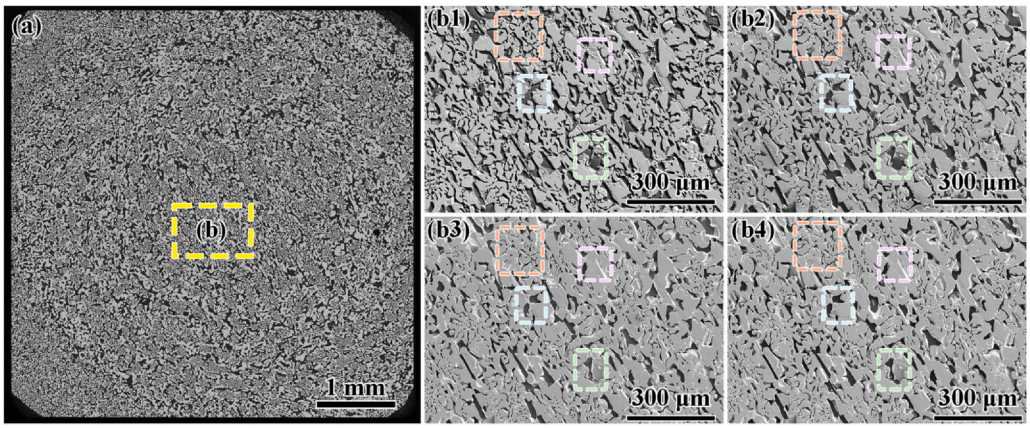

Fig. 4. (a) Surface morphology of 10HE prior to exposure to water vapor at 1500˚C; Enlarged views of surface morphology at center region of 10HE, corresponding to area marked by yellow dashed box in (a), after exposure to water vapor corrosion at 1500˚C for: (b1) 50 h, (b2) 100 h, (b3) 150 h and (b4) 200 h.

regions following exposure to water vapor corrosion at 1500˚C: a rough region (indicated by light purple boxes in Fig. 4(b1-b4)) at coarse ($5RE_{0.2}$)AG phase and a smooth region (indicated by light orange boxes in Fig. 4(b1-b4) at fine ($5RE_{0.2}$)AG phase. This suggest that at 1500˚C in a water vapor environment, high-entropy ($5RE_{0.2}$)AG phase underwent a re-sintering process. Additionally, corrosion pits associated with Al_2O_3 phase become progressively pronounced with prolonged exposure time from 50 to 200 h, as highlighted by light green boxes in Fig. 4(b1-b4). This indicates that under 1500˚C water vapor environment, Al_2O_3 phase in REAG/Al_2O_3 DSE ceramics is more susceptible to corrosion, whereas garnet phase demonstrates considerably better corrosion resistance.

Similarly, secondary electron images and EDS elemental mappings of selected area in 10HE surface before and after exposure to water vapor corrosion at 1500˚C are presented in Fig. 5. These results indicate that five rare earth elements (Y, Gd, Ho, Er and Yb) are predominantly located within ($5RE_{0.2}$)AG phase. To quantitatively assess influence of five rare earth elements during water vapor corrosion process at 1500˚C, EDS point analysis was conducted on sample surface before and after 200-hour corrosion period. These results reveal that, prior to water vapor corrosion, Gd content and total concentration of five rare earth elements in ($5RE_{0.2}$)AG phase is 3.14 at% and 15.76 at%, respectively. Following water vapor corrosion at 1500˚C, ($5RE_{0.2}$)AG phase exhibits differentiation into two distinct regions: a rough region and a smooth region, as indicated by light purple and light orange boxed in Fig. 4(b1-b4). In rough region, Gd and the total rare earth elements contents are 4.14 at% and 17.34 at%, respectively. Whereas in smooth region, the corresponding values are measured to be 2.71 at% and 16.42 at%, respectively. These findings suggest that the other four elements (Y, Ho, Er and Yb) are more susceptible to corrosion, resulting in a higher concentration of Gd remaining in the rough regions. Among these (Fig. 5(a-e)), Y, Ho, Er and Yb elements exhibit a uniform distribution both prior to and following high-temperature water vapor corrosion. When compared with other four rare-earth elements (Y, Ho, Er and Yb) in high-entropy ($5RE_{0.2}$)AG phase, the pronounced enrichment of Gd element at corrosion surface and edge of high-entropy ($5RE_{0.2}$)AG phase (Fig. 5) suggests that among five rare-earth elements, Gd possesses the largest ionic radius, resulting in the slowest diffusion rate. Consequently, during re-sintering and corrosion processes, it separates from ($5RE_{0.2}$)AG phase at the slowest speed compared with other four rare-earth elements. Additionally, as evidenced by the distribution patterns of Al and O in Fig. 5(a-e), Al_2O_3 phase undergoes progressive degradation over time. By combing EDS elemental mappings of Al and O with secondary electron images, it is observed that regions initially dominated by Al and O elements are gradually replaced by corrosion pits. This result suggests a strong correlation between the formation of corrosion pits on surface of REAG/Al_2O_3 DSE ceramics and the presence of Al_2O_3 phase. Accordingly, Al_2O_3 phase and associated corrosion pits are collectively evaluated as an integrated entity, referred to as Al_2O_3/pits, on surface of REAG/Al_2O_3 DSE ceramics following exposure to water vapor.

As illustrated in Fig. 2, weight change of 300HE after being exposed to water vapor at 1500˚C for 200 h is slightly lower than that of 10HE under identical conditions. Fig. 6(a) further presents the surface morphology of 300HE sample prior to water vapor exposure, along with magnified views of the region indicated by yellow dashed box (b) in

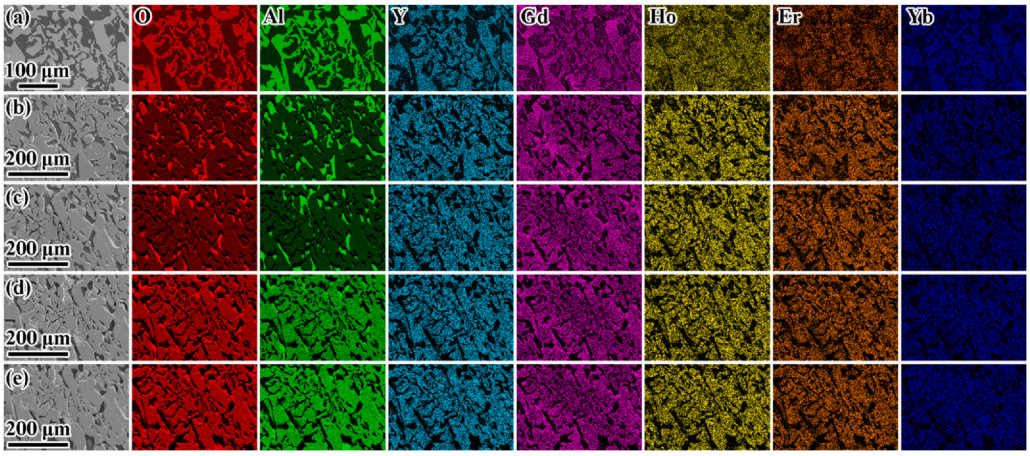

Fig. 5. Secondary electron images and corresponding EDS elemental mappings of 10HE surface subjected to water vapor corrosion at 1500˚C for varying durations: (a) 0 h, (b) 50 h, (c) 100 h, (d) 150 h and (e) 200 h.

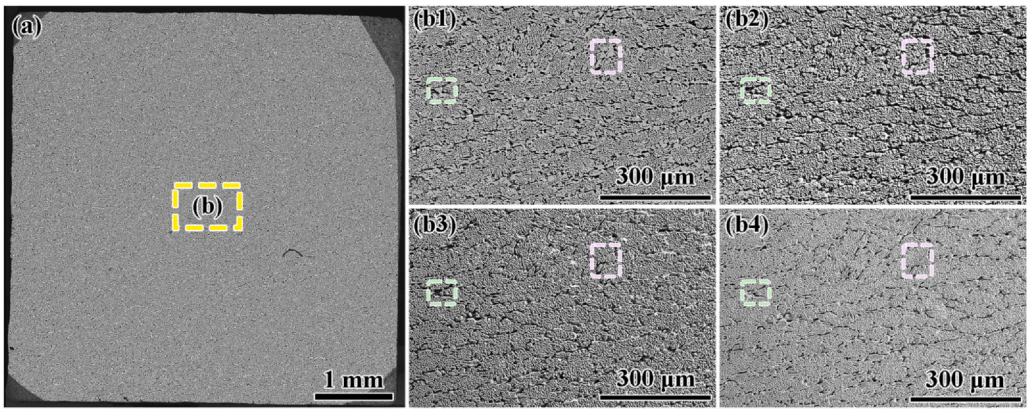

Fig. 6. (a) Surface morphology of 300HE prior to exposure to water vapor at 1500°C; Enlarged views of surface morphology at center region of 300HE, corresponding to area marked by yellow dashed box in (a), after exposure to water vapor corrosion at 1500°C for: (b1) 50 h, (b2) 100 h, (b3) 150 h and (b4) 200 h.

Fig. 6(a), captured before and after exposure to water vapor at 1500°C, with the objective of analyzing its behavior under these conditions. As shown in Fig. 6(a), the microstructure of 300HE exhibits an irregular "Chinese Script"-type eutectic structure composed of grey and black phases. According to EDS analysis, grey phase primarily consists of five RE elements, along with Al and O. The molar ratio of RE elements to Al is about 3:5.1, indicating that the grey phase corresponds to $(5RE_{0.2})AG$ phase. Meanwhile the black phase is composed of Al and O with a molar ratio of 2:2.8, indicating it corresponds to Al_2O_3 phase. Initially, after a 50-hour water vapor exposure (Fig. 6(b1)), the fine Al_2O_3 phase in 300HE was nearly completely corroded, leading to the formation of corrosion pits. Additionally, coarse Al_2O_3 phase presented a decreasing trend. Meanwhile, the surface of $(5RE_{0.2})AG$ phases in 300HE exhibit signs of corrosion accompanied by slight surface roughening, as depicted by light purple boxes in Fig. 6(b1-b4). With the prolongation of corrosion duration, the extent of degradation within Al_2O_3 phase progressively intensifies. Moreover, coarse Al_2O_3 phase demonstrates a gradually increasing degree of corrosion (as indicated by light green boxes in Fig. 6(b1-b4)).

To quantitatively analyze the distribution of the five rare earth constituent elements during water vapor corrosion, EDS analysis was performed on $(5RE_{0.2})AG$ phase at surface of 300HE specimens before and after exposure to water vapor at 1500°C. The results show that atomic concentrations of Gd and the total of five rare earth elements in $(5RE_{0.2})AG$ phase are 3.23 at% and 15.78 at% before corrosion, and 3.80 at% and 15.25 at% after 50 h of water vapor corrosion at 1500°C, respectively. A slight increase in Gd content within $(5RE_{0.2})AG$ phase following 50 h of water vapor exposure at 1500°C suggests minor corrosion and volatilization of other four rare earth elements (Y, Ho, Er and Yb) present in surface $(5RE_{0.2})AG$ phase. Furthermore, EDS elemental mapping results were performed on 300HE specimens before and after exposure, with results presented in Fig. 7. Fig. 7(a) reveals that the five RE elements are predominantly distributed within $(5RE_{0.2})AG$ phase, but with distinct distribution patterns. Specifically, Y, Ho, Er and Yb exhibit a relatively uniform distribution, whereas Gd demonstrates localized segregation within certain coarse $(5RE_{0.2})AG$ phase. Subsequently, as corrosion duration increased, the distribution of Gd elements within $(5RE_{0.2})AG$ phase gradually became more homogeneous, with only slight segregation observed at interface regions, as shown in Fig. 7(b-e). Therefore, interfacial regions of $(5RE_{0.2})AG$ phase are most susceptible to severe corrosion under water vapor exposure at 1500°C, as evidenced by slight Gd segregation at interfacial region of $(5RE_{0.2})AG$, a behavior consistent with that observed in 10HE sample. The remaining four RE elements retained a uniform distribution following high-temperature water vapor corrosion, as depicted in Fig. 7(b-e). It is noteworthy that, according to elemental distribution maps of O and Al, after 50 h of water vapor corrosion (Fig. 7(b)), Al_2O_3 phase on surface of 300HE was largely consumed. Upon extending corrosion duration to 100 h, Al_2O_3 phase became nearly undetectable, indicating that the extent of corrosion had exceeded detection depth of the EDS analysis.

Fig. 8 presents the surface morphologies of 10YA before and after water vapor corrosion at 1500°C. As illustrated in Fig. 8(a), 10YA sample displays a "Chinese Script"-like microstructure characterized by intertwined and coupled growth arrangement of grey and black phases. EDS analysis reveals that grey phase contains Y, Al and O elements,

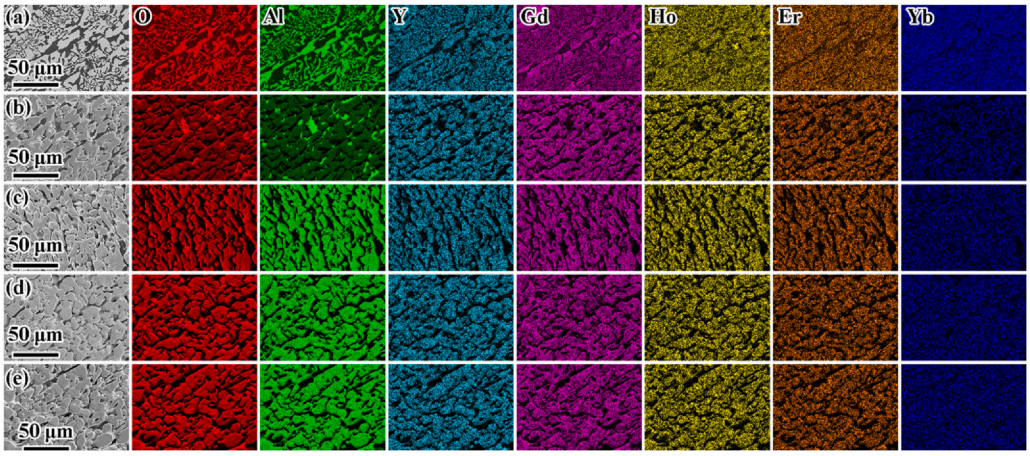

Fig. 7. Secondary electron images and corresponding EDS elemental mappings of 300HE surface subjected to water vapor corrosion at 1500°C for varying durations: (a) 0 h, (b) 50 h, (c) 100 h, (d) 150 h and (e) 200 h.

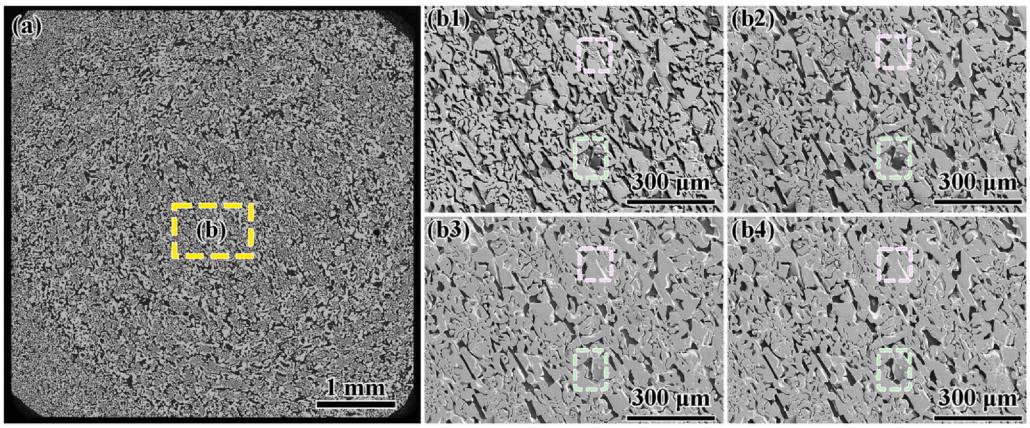

Fig. 8. (a) Surface morphology of 10YA prior to exposure to water vapor at 1500°C; enlarged views of surface morphology at center region of 10YA, corresponding to area marked by yellow dashed box in (a), after exposure to water vapor corrosion at 1500°C for: (b1) 50 h, (b2) 100 h, (b3) 150 h and (b4) 200 h.

with a Y-to-Al atomic ratio of 3:4.8, which aligns with stoichiometric composition of YAG phase. Besides, the black phase consists exclusively of Al and O, with an atomic ratio of 2:2.8, confirming its identification as Al_2O_3 phase. From magnified images of central regions of 10YA sample surface (Fig. 8(b1-b4)) marked by yellow dashed box (b) in Fig. 8(a), it is evident that Al_2O_3 phase underwent progressive corrosion with increasing exposure time (as indicated by light green boxes), while YAG phase exhibited only a slight degree of roughness (as indicated by light purple boxes). Upon comparing the surfaces of 10HE, 300HE and 10YA samples after their exposure to water vapor corrosion at 1500°C, as depicted in Figs. 4, 6, and 8, it can be observed that the surface of single-component YAG phase is smoother than that of high-entropy $(5RE_{0.2})AG$ phase. This finding indicates that the corrosion and re-sintering process of single-component YAG phase in a 1500°C water vapor environment is more uniform when compared to that of high-entropy $(5RE_{0.2})AG$ phase.

Additionally, the average widths of REAG lamellar and Al_2O_3/pits in central regions of three samples 10HE, 300HE and 10YA, before and after exposure to water vapor corrosion at 1500°C for varying durations, was quantitatively determined using MIPAR (v5.0.0) image analysis software, as summarized in Table 1. This analysis aimed to further investigate water vapor corrosion behavior of REAG/Al_2O_3 DSE ceramics. The average widths of $(5RE_{0.2})AG$ lamellar and Al_2O_3 lamellar in 10HE sample prior to water vapor corrosion were determined to be 15.79 μm and 12.75 μm, respectively. Besides, the average width values of $(5RE_{0.2})AG$ and Al_2O_3/pits in 10HE sample after exposure to water vapor corrosion for 50 h, 100 h,150 h and 200 h were determined to be 17.71 μm and 9.75 μm, 19.35 μm and 9.03 μm, 20.42 μm and 8.43 μm, as well as 21.26 μm and 7.99 μm, respectively. Moreover, the average widths of $(5RE_{0.2})AG$ lamellar and Al_2O_3 lamellar in 300HE sample before experiment of water vapor were measured as 3.44 μm and 2.77 μm, respectively. Subsequently, the average lamellar widths of $(5RE_{0.2})AG$ and Al_2O_3/pits in 300HE sample, after undergoing water vapor corrosion for 50, 100,150 and 200 h, were measured to be 6.34 μm and 2.43 μm, 8.15 μm and 1.97 μm, 12.66 μm and 2.16 μm, as well as 14.04 μm and 1.95 μm, respectively. Additionally, in 10YA sample, the average lamellar widths of $(5RE_{0.2})AG$ phase and Al_2O_3 phase were 4.18 μm and 3.38 μm before water vapor corrosion, and 5.05 μm and 2.93 μm after 50 h water vapor corrosion, 8.00 μm and 2.62 μm after 100 h, 8.09 μm and 2.37 μm after 150 h, 8.19 μm and 2.10 μm after 200 h, respectively. Following exposure to water vapor at 1500°C for 200 h, the average lamellar widths of garnet phase in 10HE, 300HE and 10YA samples increased by 34.7%, 308.8% and 96.2%, respectively. This observation suggests that during the 1500°C water vapor corrosion, garnet phases (including both high-entropy $(5RE_{0.2})AG$ phase and YAG phase) demonstrate not only surface roughening but also significant grain growth. Notably, under these conditions, the high-entropy $(5RE_{0.2})AG$ phase exhibits significantly more pronounced grain growth compared to YAG phase. These results suggest that after corrosion exposure to 1500°C water vapor environment, the high-entropy $(5RE_{0.2})AG$ phase underwent a more pronounced re-sintering and higher degree of grain growth in comparison with YAG phase. Meanwhile, within 200 h of water vapor corrosion at 1500°C, the average width of Al_2O_3 phase decreased by 37.3%, 29.7% and 37.7%, respectively, indicating a significant reduction in Al_2O_3 phase. The variation trend in the average size of Al_2O_3 phase across the three samples was found to be consistent with their respective weight loss. Therefore, a positive correlation exists between the dimensional change of Al_2O_3 in REAG/Al_2O_3 DSE ceramics and their weight loss during water vapor corrosion process.

As demonstrated in Figs. 6–8, the differing corrosion rates of garnet and alumina phases on the REAG/Al_2O_3 surface led to progressively increasing surface roughness as high-temperature water vapor corrosion progresses. To quantitatively characterize the disparity in corrosion loss between garnet and Al_2O_3 phases, we conducted a comparative analysis of surface roughness variations across three samples (10HE, 300HE and 10YA) using laser scanning confocal microscopy, and the results are presented in Fig. 9. It is seen that the surfaces of

Table 1
The average widths of REAG/Al_2O_3 lamellar in 10HE, 300HE and 10YA before and after exposure to water vapor at 1500°C.

Time (h)	Average lamellar width (μm)					
	10HE		300HE		10YA	
	Garnet	Al_2O_3/Pits	Garnet	Al_2O_3/Pits	Garnet	Al_2O_3/Pits
0	15.79	12.75	3.44	2.77	4.18	3.38
50	17.71	9.75	6.34	2.43	5.05	2.93
100	19.35	9.03	8.15	1.97	8.00	2.62
150	20.42	8.43	12.66	2.16	8.09	2.37
200	21.26	7.99	14.04	1.95	8.19	2.10

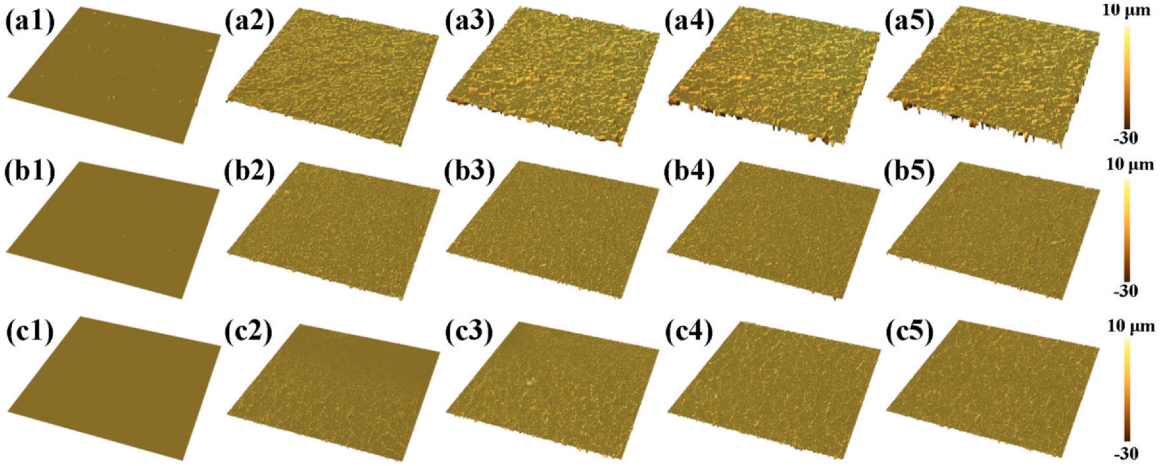

Fig. 9. Laser scanning confocal microscope images obtained from water vapor corrosion tests conducted at 1500°C for three different samples over various exposure durations: (a1-a5) 10HE, (b1-b5) 300HE and (c1-c5) 10YA; where (a1-c1) correspond to 0 h, (a2-c2) to 50 h, (a3-c3) to 100 h, (a4-c4) to 150 h and (a5-c5) to 200 h of exposure time.

10HE, 300HE and 10YA appeared essentially flat following grinding and polishing and prior to exposure to high-temperature water vapor corrosion, with no significant surface undulations observed, as presented in Fig. 9(a1-c1). Upon prolonged exposure to water vapor corrosion, all samples, including 10HE (Fig. 9(a2-a5)), 300HE (Fig. 9(b2-b5)) and 10YA (Fig. 9(c2-c5)), exhibited a marked increase in surface undulation. A comparison of surface topography of three samples under identical water vapor exposure conditions, as depicted in Fig. 9(a2-c2), (a3-c3), (a4-c4) and (a5-c5), reveals that surface undulation was most pronounced in 10HE (Height differential before and after water vapor corrosion $\Delta h = 26.56$ μm), followed by 10YA ($\Delta h = 19.09$ μm), while 300HE ($\Delta h = 16.06$ μm) exhibited the least degree of surface undulation. This trend is consistent with the weight loss results shown in Fig. 2.

Additionally, the surface roughness of all three samples was quantitatively evaluated by calculating both the arithmetic average roughness (S_a) and root-mean-square roughness(S_q), and results are summarized in Fig. 10. The magnitudes of these two indicators are directly correlated with the degree of surface roughness. Smaller values of S_a and S_q indicate smoother microscopic undulations on object's surface and lower roughness; conversely, larger values of S_a and S_q signify more intense microscopic undulations on surface and higher roughness. As evident from the data, both parameters exhibited comparable trends during the corrosion process, showing an increasing tendency with prolonged exposure duration. Consequently, in subsequent analysis of roughness variations, S_a was selected as representative parameter for discussion. As shown in Fig. 10(a), after 50 h of exposure to water vapor corrosion at 1500°C, surface roughness of 10HE increased significantly from 0.113 μm to 1.966 μm, representing an approximate 17.4-fold rise. Subsequently, during corrosion periods from 50 to 100 h, from 100 to 150 h, and from 150 to 200 h, surface roughness further increased to 3.373 μm, 4.537 μm and 5.017 μm, respectively, corresponding to additional increases by factors of 1.7, 1.3 and 1.1. These findings indicate that over 200-hour water vapor corrosion period, Al_2O_3 phase in 10HE underwent progressive degradation, with the most substantial deterioration occurring within initial 50 h. Additionally, initial surface roughness of 300HE (Fig. 10(b)) was measured at 0.104 μm. After 50 h of exposure to water vapor corrosion, the surface roughness increased to 0.691 μm, representing a 6.6-fold increase. Between 50 and 100 h of corrosion, surface roughness further rose to 1.241 μm, indicating an additional increase of 0.550 μm. However, from 100 to 150 h, a slight reduction in surface roughness was observed, returning to 1.207 μm. Finally, within time range from 150 to 200 h, surface roughness increased further to 1.253 μm. These findings suggest that the consumption of majority of surface Al_2O_3 phase in 300HE occurred within 100 h. In subsequent stages of water vapor corrosion (from 100 h to 200 h), surface alterations became increasingly stable, resulting in only minor fluctuations in surface roughness, which remained essentially unchanged. For 10YA sample (Fig. 10(c)), surface roughness progressively increased over four-time intervals, namely 0–50 h, 50–100 h, 100–150 h and 150–200 h. It increased from 0.044 μm to 0.652 μm, from 0.652 μm to 1.090 μm, from 1.090 μm to 1.100 μm, and further to

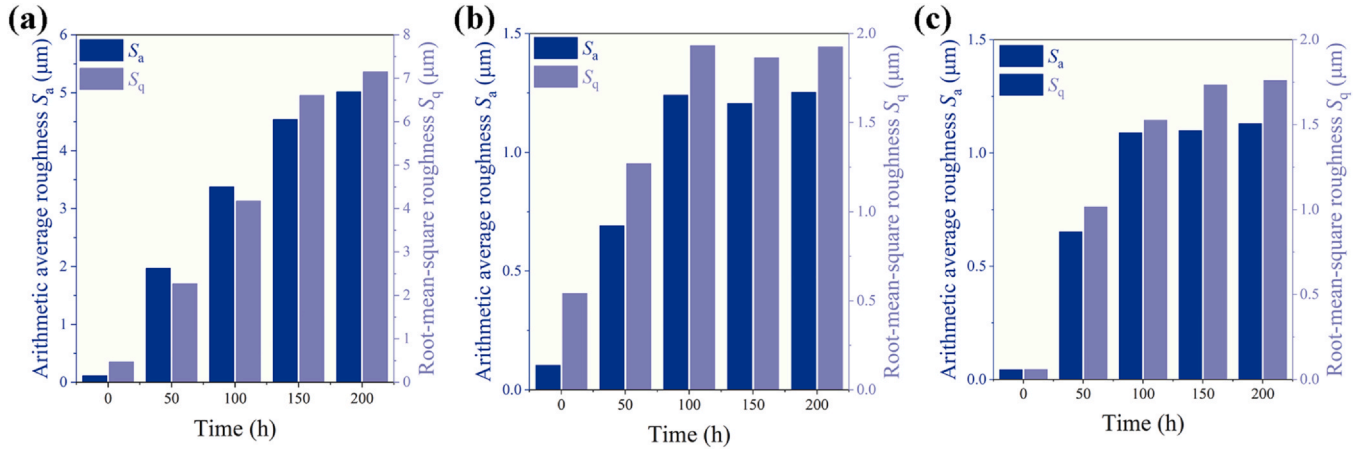

Fig. 10. Surface roughness of REAG/Al_2O_3 DSE ceramics following water vapor corrosion testing at 1500°C for various durations: (a) 10HE, (b) 300HE and (c) 10YA.

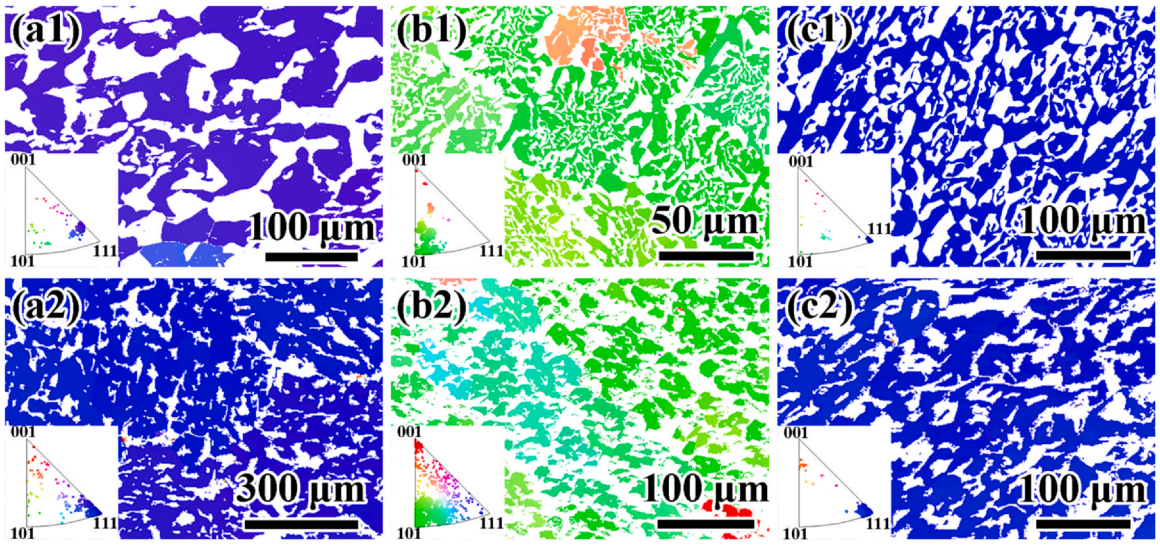

Fig. 11. Representative surface EBSD analysis of garnet on sample surfaces: (a1-a2) 10HE, (b1-b2) 300HE and (c1-c2) 10YA, conducted (a1-c1) prior to and (a2-c2) following exposure to water vapor corrosion at 1500˚C.

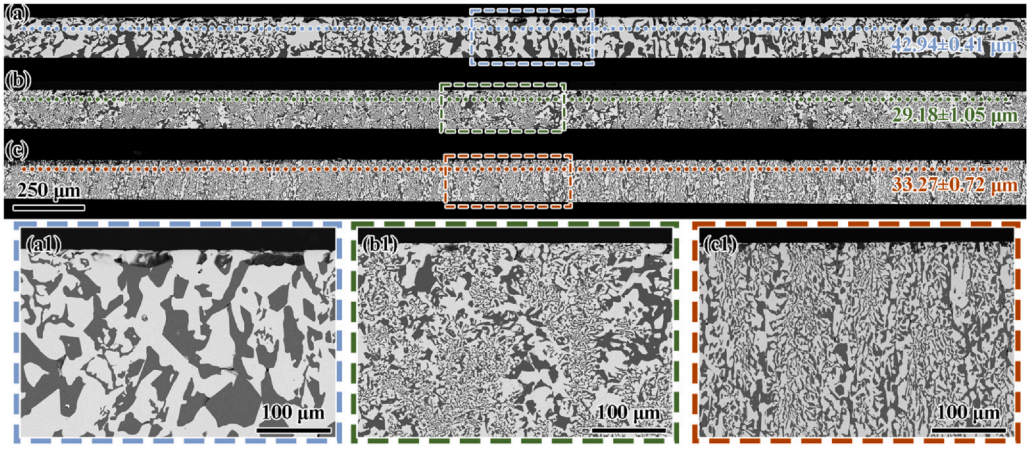

Fig. 12. Cross-sectional microstructures of (a) 10HE, (b) 300HE and (c) 10YA after exposure to water vapor at 1500˚C; (a1) magnified view of central region marked in (a), (b1) magnified view of central region marked in (b), and (c1) magnified view of central region marked in (c), respectively.

1.130 μm, representing approximately increases of 14.8-fold, 1.8-fold, 1.0-fold and 1.0-fold, respectively. These results indicate that 10YA exhibits significant corrosion primarily within 100 h when it is exposed to a high-temperature water vapor environment. Moreover, based on the surface roughness data presented in Fig. 10, it can be inferred that after water vapor corrosion at 1500˚C for 200 h, the 10HE, 300HE and 10YA samples exhibited surface roughness increases to 44.4, 12.0, and 25.7 times their initial values, respectively.

To further investigate the corrosion behavior of REAG/Al_2O_3 DSE ceramics under water vapor exposure at 1500˚C, the crystallographic orientations of the surface before and after exposure were analyzed using electron backscatter diffraction. Fig. 11 presents the representative EBSD patterns of garnet phase on surface of REAG/Al_2O_3 DSE ceramics before and after exposure to water vapor at 1500˚C. It should be noted that after exposure to water vapor at 1500˚C, Al_2O_3 phase on surface of REAG/Al_2O_3 DSE ceramics was nearly entirely consumed, as evidenced by Figs. 4, 6 and 8. Consequently, EBSD characterization of corroded surface failed to detect the presence of the Al_2O_3 phase after high-temperature water vapor corrosions. Therefore, this section focuses solely on orientation evolution of garnet phase, while analysis of orientation changes in Al_2O_3 phase is discussed in Section 3.4. As illustrated in Fig. 11(a1-a2), ($5RE_{0.2}$)AG phase in 10HE exhibits a preferred orientation along < 111 > direction both before and after exposure to water vapor corrosion at 1500˚C. In contrast, ($5RE_{0.2}$)AG phase in 300HE predominantly displays a preferred orientation along < 110 > direction before and after water vapor corrosion (Fig. 11(b1-b2)). Additionally, YAG phase in 10YA maintains its preferred orientation along < 111 > direction following high-temperature water vapor corrosion (Fig. 11(c1-c2)). These findings indicate that water vapor corrosion at 1500˚C does not significantly alter the crystallographic orientation of garnet phase in REAG/Al_2O_3 DSE ceramics, implying that garnet phase experiences minimal water vapor corrosion preferentially along its original orientation.

3.4. Cross-sectional microstructure

Corrosion of Al_2O_3 phase under water vapor environment at 1500˚C resulted in the formation of corrosion pits, which facilitated a progressive inward advancement of corrosion front. After 200 h of exposure to water vapor, surface corrosion interface became indiscernible. To further investigate the characteristics of corrosion interface under water vapor conditions, three samples 10HE, 300HE and 10YA were sectioned at their central position and subjected to cross-sectional analysis. Fig. 12 illustrates cross-sectional microstructures of 10HE, 300HE and 10YA following exposure to water vapor at 1500˚C. Moreover, Fig. 12(a1-c1) provides magnified views of central regions marked in corresponding full cross-sectional microstructures. As illustrated in Fig. 12(a-c), the maximum corrosion depths of corrosion pits for 10HE,

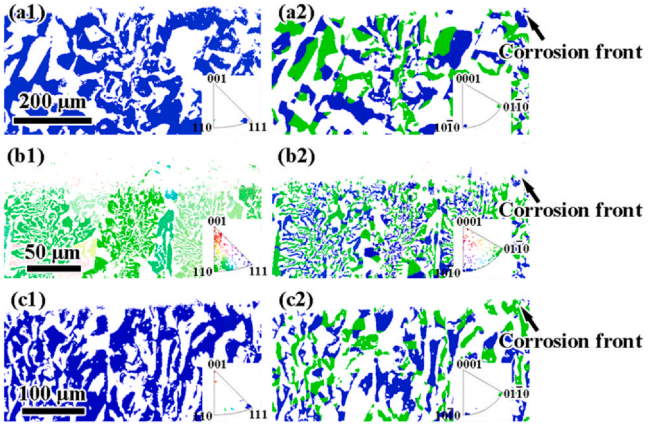

Fig. 13. Representative EBSD analysis of cross-section for (a1-a2) 10HE, (b1-b2) 300HE and (c1-c2) 10YA after exposure to water vapor at 1500°C; (a1-c1) $(5RE_{0.2})AG$ and (a2-c2) Al_2O_3.

300HE and 10YA are approximately 42.94 ± 0.41 μm, 29.18 ± 1.05 μm and 33.27 ± 0.72 μm, respectively. A comparison of corrosion depths in conjunction with average lamellar widths of Al_2O_3 phase presented in Table 1 indicates that extent of corrosion is influenced by widths of Al_2O_3 lamellar, revealing a nearly linear positive correlation between average lamellar widths of Al_2O_3 phase and maximum corrosion depth. To be more specific, the corrosion depth of sample surface increases progressively with average lamellar widths of Al_2O_3 phase. Moreover, linear fitting was performed on data related to change in surface roughness and maximum corrosion depth. The calculated coefficient of determination (R^2) attains value of 0.9, suggesting a positive correlation between change in surface roughness and maximum corrosion depth. Further observations of magnified views of central region in 10HE (Fig. 12(a1)), 300HE (Fig. 12(b1)) and 10YA (Fig. 12(c1)) reveal that corrosion-affected areas predominantly consist of garnet phase. The corrosion interface is composed of either garnet phase or a residual trace amount of Al_2O_3 phase, which means garnet phase serves as structural framework responsible for maintaining structural integrity of $REAG/Al_2O_3$ DSE ceramics under high-temperature water vapor conditions.

To investigate the evolution of crystallographic orientation of the REAG and Al_2O_3 phases in cross-sectional samples, EBSD was also employed to analyze the crystallographic orientation of cross sections after exposure to water vapor at 1500°C, and the results are shown in Fig. 13. The garnet phase in the 10HE, 300HE, and 10YA samples exhibits a consistent crystallographic orientation from matrix to corrosion front. The preferred orientations along growth direction are < 111 >, < 110 >, and < 111 >, respectively. While Al_2O_3 phase in corresponding regions of all three sample groups consistently displays a stable $< 10\bar{1}0 >$ preferred orientation along growth direction. It should be noted that green and blue colors in Al_2O_3 phase, corresponding to $< 10\bar{1}0 >$ and $< 01\bar{1}0 >$ crystallographic orientations, respectively, represent two twin-related variants that are not strictly equivalent, however, EBSD is unable to distinguish between them [38]. These findings indicate that water vapor corrosion at 1500°C does not significantly alter crystallographic orientations of garnet and Al_2O_3 phase in $REAG/Al_2O_3$ DSE ceramics.

Based on the aforementioned discussions regarding weight loss, corrosion surface and corrosion cross-section, a simulation analysis of water vapor behavior of the exposed surface of high-entropy $(5RE_{0.2})AG/Al_2O_3$ DSE ceramics at 1500°C is further conducted. Prior to conducting water vapor corrosion experiment, the surface of high-entropy $(5RE_{0.2})AG/Al_2O_3$ DSE ceramic was ground and polished to achieve a smooth and flat finish. $(5RE_{0.2})AG$ phase and Al_2O_3 phase exhibited a uniform and irregular eutectic morphology, forming an interpenetrating network structure in three-dimensional space, as depicted in Fig. 14(a). After subjected to water vapor corrosion, both $(5RE_{0.2})AG$ phase and Al_2O_3 phase on the surface reacted with water vapor to generate gaseous hydroxide products. Owing to the higher reaction rate of Al_2O_3 phase with water vapor compared to that of $(5RE_{0.2})AG$ phase, the majority of Al_2O_3 phase on surface was completely corroded, leaving only $(5RE_{0.2})AG$ phase. Simultaneously, the re-sintering of high-entropy $(5RE_{0.2})AG$ phase resulted in an increase in surface undulation, as shown in Fig. 14(b). Furthermore, as corrosion time prolonged, surface Al_2O_3 phase undergoes further corroded over time. Meanwhile, remaining $(5RE_{0.2})AG$ phase can maintain structural stability, as demonstrated in Fig. 14(c).

4. Conclusions

This study investigates corrosion behavior of $REAG/Al_2O_3$ DSE ceramics, including high-entropy $(5RE_{0.2})AG/Al_2O_3$ DSE ceramics fabricated at growth rates of 10 mm/h and 300 mm/h, and YAG/Al_2O_3 DSE ceramic grown with 10 mm/h, under a water vapor environment consisting of 90 $H_2O_{(g)}$ and 10 vol% $Air_{(g)}$ at 1500°C over exposure durations ranging from 50 to 200 h. The key findings of this research are summarized as follows:

(1) The $REAG/Al_2O_3$ DSE ceramics demonstrated excellent resistance to water vapor corrosion after exposure at 1500°C for 200 h. The amount of Al_2O_3 phase on surface gradually decreased over time. Consequently, mass loss gradually increases as time progresses. When time reaches 200 h, mass loss of three samples (10HE, 300HE and 10YA) range from 0.00708 $mg{\cdot}cm^{-2}{\cdot}mg^{-1}$ to 0.00757 $mg{\cdot}cm^{-2}{\cdot}mg^{-1}$.
(2) Under the water vapor corrosion at 1500°C, Al_2O_3 phase serves as corrosion-susceptible component in $REAG/Al_2O_3$ DSE ceramics, whereas garnet phase acts as corrosion-inert and structurally stable phase. The extent of water vapor corrosion in $REAG/Al_2O_3$ DSE ceramics is strongly correlated with eutectic microstructure like interspaces and the widths of eutectic lamellar, exhibiting a nearly linear positive relationship between maximum corrosion depth and lamellar widths of Al_2O_3 phases.

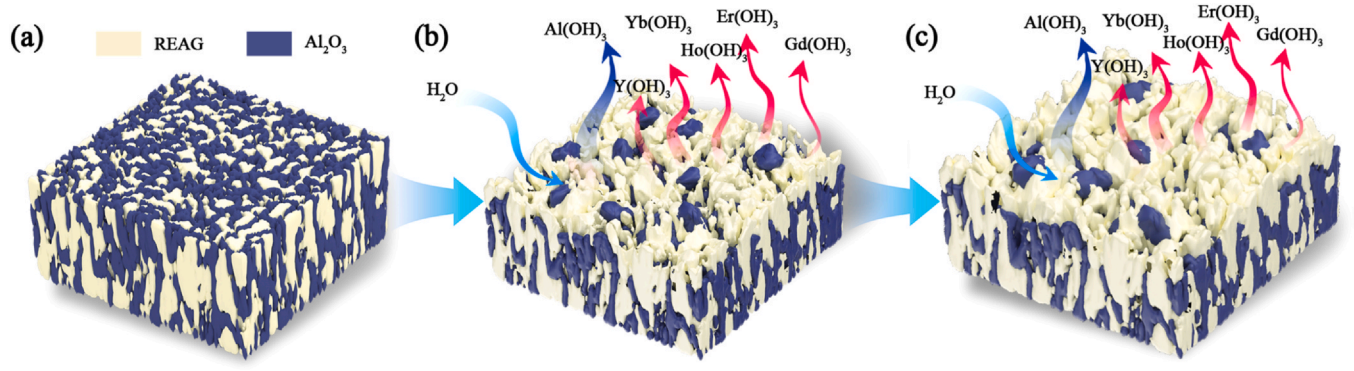

Fig. 14. Schematic illustration of time-dependent water vapor corrosion behavior on high-entropy $(5RE_{0.2})AG/Al_2O_3$ DSE ceramic at 1500°C.

(3) The multiple rare-earth elements in high-entropy $(Y_{0.2}Gd_{0.2}Ho_{0.2}Er_{0.2}Yb_{0.2})_3Al_5O_{12}$ exhibit variations in corrosion resistance at 1500°C, with Gd demonstrating the slowest diffusion rate among other four elements. Nevertheless, the preferred orientations of garnet phase in 10HE, 300HE and 10YA samples remain consistent at < 111 > , < 110 > and < 111 > , respectively. This indicates that the crystallographic orientation stability of garnet phase is preserved under water vapor exposure at 1500°C, suggesting that controlling crystallographic orientation can enhance the resistance of REAG/Al_2O_3 DSE ceramics to high-temperature water vapor corrosion.

CRediT authorship contribution statement

Cui Zhou: Writing – original draft, Methodology, Investigation. **Zhilin Tian:** Methodology, Investigation. **Liya Zheng:** Methodology, Investigation. **Sikai Wang:** Investigation. **Tiefeng Du:** Investigation. **Jiemin Wang:** Methodology. **Yang Bing:** Funding acquisition. **Luchao Sun:** Writing – review & editing, Supervision, Funding acquisition, Conceptualization. **Jingyang Wang:** Writing – review & editing, Supervision, Funding acquisition, Conceptualization. **Min Guo:** Funding acquisition, Investigation.

Declaration of Competing Interest

The authors declare that they have no known competing financial interests or personal relationships that could have appeared to influence the work reported in this paper.

Acknowledgement

Thanks for supports from the National Key R&D Program of China (2024YFB3714504); National Natural Science Foundation of China (52130204, U21A2063); LiaoNing Revitalization Talents Program (XLYC2203090); International Partnership Program of the Chinese Academy of Sciences (172GJHZ2022094FN).

References

[1] S. Krämer, J. Yang, C.G. Levi, C.A. Johnson, Thermochemical interaction of thermal barrier coatings with molten CaO-MgO-Al_2O_3-SiO_2 (CMAS) deposits, J. Am. Ceram. Soc. 89 (2006) 3167–3175.
[2] J. Li, Z.X. Luo, Y. Cui, G.H. Zhang, L.C. Sun, J.Y. Wang, CMAS corrosion resistance of $Y_3AlS_5O_{12}/Al_2O_3$ ceramic coating deposited by atmospheric plasma spraying, J. Inorg. Mater. 39 (2024) 671–680.
[3] E.J. Opila, Oxidation and volatilization of silica formers in water vapor, J. Am. Ceram. Soc. 86 (2004) 1238–1248.
[4] J. Zhang, R.J. Liu, Y.J. Jian, F. Wan, Y.F. Wang, Degradation mechanism of SiC_f/SiC composites after long-time water vapor and oxygen corrosion at 1300°C, Corros. Sci. 197 (2022) 110099.
[5] Y. Waku, N. Nakagawa, T. Wakamoto, H. Ohtsubo, K. Shimizu, Y. Kohtok, A ductile ceramic eutectic composite with high strength at 1873 K, Nature 389 (1997) 49–52.
[6] A. Henniche, J.H. Ouyang, Y.H. Ma, Z.G. Wang, Y.J. Wang, Z.G. Liu, Microstructure and mechanical properties of ceramics obtained from chemically co-precipitated Al_2O_3-$GdAlO_3$ nano-powders with eutectic composition, Ceram. Int. 43 (2017) 6996–7001.
[7] S. Yan, D.J. Wu, Y.F. Huang, N. Liu, Y.N. Zhang, F.Y. Niu, G.Y. Ma, C fiber toughening Al_2O_3-ZrO_2 eutectic via ultrasonic-assisted directed laser deposition, Mater. Lett. 235 (2019) 228–231.
[8] D.G. Liu, Y. Gao, J.L. Liu, F.Z. Liu, K. Li, H.J. Su, Y.G. Wang, L.N. An, Preparation of Al_2O_3-$Y_3Al_5O_{12}$-ZrO_2 eutectic ceramic by flash sintering, Scr. Mater. 114 (2016) 108–111.
[9] S.Y. Zhai, J.C. Liu, Q. Liu, Changes in the microstructure and mechanical properties of Al_2O_3/YSZ directionally solidified eutectic ceramics during long-time heat treatment, J. Eur. Ceram. Soc. 41 (2021) 266–273.
[10] H.J. Su, Z.L. Shen, W.D. Ma, Y. Liu, D. Zhao, Y.N. Guo, Comprehensive microstructure regularization mechanism and microstructure-property stability at 1773K of directionally solidified Al_2O_3/$GdAlO_3$ eutectic ceramic composite, Compos. B Eng. 256 (2023) 110647.
[11] Y. Waku, N. Nakagawa, T. Wakamoto, H. Ohtsubo, K. Shimizu, Y. Kohtoku, High-temperature strength and thermal stability of a unidirectionally solidified Al_2O_3/YAG eutectic composite, J. Mater. Sci. 33 (1998) 1217–1225.
[12] M.C. Mesa, S. Serrano-Zabaleta, P.B. Oliete, A. Larrea, Microstructural stability and orientation relationships of directionally solidified Al_2O_3-$Er_3Al_5O_{12}$-ZrO_2 eutectic ceramics up to 1600°C, J. Eur. Ceram. Soc. 34 (2014) 2071–2080.
[13] H.J. Su, E.Y. Wang, Q. Ren, H.F. Liu, D. Zhao, G.Y. Fan, J. Zhang, L. Liu, H.Z. Fu, Microstructure tailoring and thermal stability of directionally solidified Al_2O_3/$GdAlO_3$ binary eutectic ceramics by laser floating zone melting, Ceram. Int. 44 (2018) 7908–7916.
[14] M.C. Mesa, P.B. Oliete, V.M. Orera, J.Y. Pastor, A. Martín, J. Llorca, Microstructure and mechanical properties of $Al_2O_3/Er_3Al_5O_{12}$ eutectic rods grown by the laser-heated floating zone method, J. Eur. Ceram. Soc. 31 (2011) 1241–1250.
[15] S.Q. Hao, H.J. Su, D. Zhao, X. Li, Z.L. Shen, Y. Liu, Y.N. Guo, Z. Zhang, M. Guo, Complex shaped Al_2O_3/YAG/ZrO_2 eutectic ceramics with excellent high temperature mechanical properties printed by vat photopolymerization, Addit. Manuf. 101 (2025) 104703.
[16] H.F. Sun, L.C. Sun, X.M. Ren, C. Zhou, J. Li, T.F. Du, J. Liu, J.Y. Wang, Outstanding molten calcium-magnesium-aluminosilicate (CMAS) corrosion resistance of directionally solidified $Al_2O_3/Y_3Al_5O_{12}$ eutectic ceramic at 1500°C, Corros. Sci. 220 (2023) 111289.
[17] X. Tan, H.J. Su, Y. Liu, J.T. Yao, H.L. Gao, H. Jiang, M.H. Yu, X. Li, P.X. Yang, Z. Zhang, M. Guo, CMAS corrosion resistance and mechanism of directionally solidified Al_2O_3/YAG eutectic ceramics at high temperatures of 1300-1500°C, Corros. Sci. 248 (2025) 112793.
[18] Y. Liu, H.J. Su, Z.L. Shen, D. Zhao, Y.N. Guo, X. Li, H. Jiang, D. Dong, C.B. Yang, High temperature calcium-magnesium-alumina-silicate (CMAS) corrosion behavior of directionally solidified Al_2O_3/YAG eutectic ceramic, J. Mater. Sci. Technol. 165 (2023) 66–74.
[19] N. Bahlawane, T. Watanabe, Y. Waku, A. Mitani, N. Nakagawa, Effect of moisture on the high-temperature stability of unidirectionally solidified Al_2O_3/YAG eutectic composites, J. Am. Ceram. Soc. 83 (2000) 3077–3081.
[20] A. Otsuka, Y. Waku, R. Tanaka, Corrosion of a unidirectionally solidified Al_2O_3/YAG eutectic composite in a combustion environment, J. Eur. Ceram. Soc. 25 (2005) 1269–1274.
[21] C. Zhou, Z.P. Luo, T.F. Du, H.F. Sun, J.M. Wang, L.C. Sun, J.Y. Wang, Directionally solidified high-entropy $(Y_{0.2}Gd_{0.2}Ho_{0.2}Er_{0.2}Yb_{0.2})_3Al_5O_{12}/Al_2O_3$ eutectic with outstanding crystallographic texture formation capability, Scr. Mater. 220 (2022) 114939.
[22] C. Zhou, L.C. Sun, T.F. Du, Z. Wu, J.M. Wang, J.Y. Wang, Excellent calcium-magnesium-aluminosilicate corrosion resistance of high-entropy garnet/alumina directionally solidified eutectic at 1500°C, J. Am. Ceram. Soc. 107 (2024) 1748–1759.
[23] Y. Zhang, T.T. Zuo, Z. Tang, M.C. Gao, K.A. Dahmen, P.K. Liaw, Z.P. Lu, Microstructures and properties of high-entropy alloys, Prog. Mater. Sci. 61 (2014) 1–93.
[24] D.B. Miracle, O.N. Senkov, A critical review of high entropy alloys and related concepts, Acta Mater. 122 (2017) 448–511.
[25] J.W. Yeh, Recent progress in high-entropy alloys, Eur. J. Control 31 (2006) 633–648.
[26] Z.W. Xiong, K. Zhang, W.H. Liao, T.T. Liu, Y. Zhang, Z.G. Zhu, In-situ synthesis of high-entropy $Al_2O_3/RE_3Al_5O_{12}/ZrO_2$ ceramic by laser powder bed fusion with exceptional properties, J. Adv. Ceram. 13 (2024) 2004–2020.
[27] B.L. Ye, T.Q. Wen, M.C. Nguyen, L.Y. Hao, C.Z. Wang, Y.H. Chu, First-principles study, fabrication and characterization of $(Zr_{0.25}Nb_{0.25}Ti_{0.25}V_{0.25})C$ high-entropy ceramics, Acta Mater. 170 (2019) 15–23.
[28] Z.F. Zhao, H. Chen, H.M. Xiang, F.Z. Dai, X.H. Wang, W. Xu, K. Sun, Z.J. Peng, Y.C. Zhou, High-entropy $(Y_{0.2}Nd_{0.2}Sm_{0.2}Eu_{0.2}Er_{0.2})AlO_3$: a promising thermal/environmental barrier material for oxide/oxide composites, J. Mater. Sci. Technol. 47 (2020) 45–51.
[29] Z.F. Zhao, H.M. Xiang, H. Chen, F.Z. Dai, X.H. Wang, Z.J. Peng, Y.C. Zhou, High-entropy $(Nd_{0.2}Sm_{0.2}Eu_{0.2}Y_{0.2}Yb_{0.2})_4Al_2O_9$ with good high temperature stability, low thermal conductivity, and anisotropic thermal expansivity, J. Adv. Ceram. 9 (2020) 595–605.
[30] Y. Dong, K. Ren, Y.H. Lu, Q.K. Wang, J. Liu, Y.G. Wang, High-entropy environmental barrier coating for the ceramic matrix composites, J. Eur. Ceram. Soc. 39 (2019) 2574–2579.
[31] X.T. Guo, Y.L. Zhang, T. Li, P.F. Zhang, K. Shuai, J. Li, X.H. Shi, High-entropy rare-earth disilicate $(Lu_{0.2}Yb_{0.2}Er_{0.2}Tm_{0.2}Sc_{0.2})_2Si_2O_7$: A potential environmental barrier coating material, J. Eur. Ceram. Soc. 42 (2022) 3570–3578.
[32] H. Yoshida, A. Nakamura, T. Sakuma, N. Nakagawa, Y. Waku, Anisotropy in high-temperature deformation in unidirectionally solidified eutectic Al_2O_3-YAG single crystals, Scr. Mater. 45 (2001) 957–963.
[33] L.C. Sun, C. Zhou, T.F. Du, Z. Wu, Y.M. Lei, J.L. Li, H.J. Su, J.Y. Wang, Directionally solidified $Al_2O_3/Er_3Al_5O_{12}$ and $Al_2O_3/Yb_3Al_5O_{12}$ eutectic ceramics prepared by optical floating zone melting, J. Inorg. Mater. 36 (2021) 652–658.
[34] K.N. Lee, D.S. Fox, N.P. Bansal, Rare earth silicate environmental barrier coatings for SiC/SiC composites and Si_3N_4 ceramics, J. Eur. Ceram. Soc. 25 (2005) 1705–1715.
[35] H.F. Liu, H.J. Su, Z.L. Shen, H. Jiang, D. Zhao, Y. Liu, Y.N. Guo, X. Li, M. Guo, J. Zhang, L. Liu, H.Z. Fu, Formation mechanism and roles of oxygen vacancies in melt-grown Al_2O_3/$GdAlO_3$/ZrO_2 eutectic ceramic by laser 3D printing, J. Adv. Ceram. 11 (2022) 1751–1763.
[36] S. Ueno, D.D. Jayaseelan, T. Ohji, Development of oxide-based EBC for silicon nitride, Int. J. Appl. Ceram. Technol. 1 (2005) 362–373.
[37] M. Fritsch, H. Klemm, M. Herrmann, B. Schenk, Corrosion of selected ceramic materials in hot gas environment, J. Eur. Ceram. Soc. 26 (2006) 3557–3565.
[38] L. Mazerolles, N. Piquet, M.F. Trichet, L. Perrière, D. Boivin, M. Parlier, New microstructures in ceramic materials from the melt for high temperature applications, Aerosp. Sci. Technol. 12 (2008) 499–505.